Phys. Med. Biol. **45** (2000) 2497–2508. Printed in the UK PII: S0031-9155(00)10144-7

Monte Carlo simulation of dose distributions from a synchrotron-produced microplanar beam array using the EGS4 code system*

I Orion†, A B Rosenfeld‡, F A Dilmanian†, F Telang†, B Ren† and Y Namito§

† Medical Department, Brookhaven National Laboratory, Upton, NY 11973, USA
‡ University of Wollongong, Department of Physics, PO Box 1144, Wollongong, New South Wales 2500, Australia
§ KEK National Laboratory for High Energy Physics, Oho, Tsukuba-shi, Ibaraki-ken 305, Japan

E-mail: orion@bnl.gov

Received 6 December 1999, in final form 7 June 2000

Abstract. Microbeam therapy is established as a general concept for brain tumour treatment. A synchrotron based x-ray source was chosen for experimental research into microbeam therapy, and therefore new simulations were essential for investigating the therapy parameters with a proper description of the synchrotron radiation characteristics. To design therapy parameters for tumour treatments, the newly upgraded LSCAT (Low energy SCATtering) package of the EGS4 Monte Carlo simulation code was adapted to develop an accurate self-written user code for calculating microbeam radiation dose profiles with a precision of 1 μm. LSCAT is highly suited to this purpose due to its ability to simulate low-energy x-ray transport with detailed photon interactions (including bound electron incoherent scattering functions, and linear polarized coherent scattering). The properties of the synchrotron x-ray microbeam, including its polarization, source spectrum and beam penumbra, were simulated by the new user codes. Two concentric spheres, an inner sphere, defined as a brain, and a surrounding sphere, defined as a skull, represented the phantom. The microbeam simulation was tested using a 3×3 cm array beam for small treatment areas and a 6×6 cm array for larger ones, with different therapy parameters, such as beam width and spacing. The results showed that the microbeam array retained an adequate peak-to-valley ratio, of five times at least, at tissue depths suitable for radiation therapy. Dose measurements taken at 1 μm resolution with an 'edge-on' MOSFET validated the basics of the user code for microplanar radiation therapy.

1. Introduction

The resistance of normal tissue to radiation damage from microscopically thin beams of ionizing radiation was first observed in 1967 by Curtis at Brookhaven National Laboratory (BNL). Slatkin *et al* (1992) used Monte Carlo simulations to show that the dose distribution generated by an array of x-ray pencil beams damages only those tissue cells lying in the direct path of the beam.

Microbeam radiation therapy kills the endothelial cells in the path of the beam, while contiguous endothelial cells survive, thereby sparing the normal tissue. The vasculature of the tissue is regenerated by the hyperplasia of the surviving cells, which subsequently migrate,

* We would like to dedicate this manuscript to the memory of Dr Pere Spanne, who was a pioneer researcher in the field of MRT. Dr Spanne died in the Swiss-Air flight accident in 1998.

0031-9155/00/092497+12$30.00

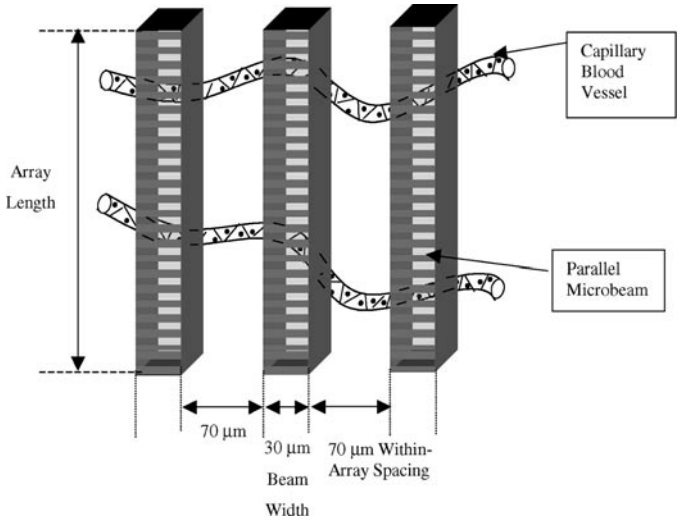

Figure 1. Illustration of an x-ray microbeam array (partial array is shown) applied to tumour tissue, in order to cut the capillaries using the unidirectional microbeam therapy method (UMRT).

divide and eventually replace the dead cells. The aim of irradiating tissue using an array of parallel narrow microbeams is to destroy the endothelial cells in the path of the beams, but to preserve the surviving cells' full viability. In the case of tumour tissue, the surviving endothelial cells cannot restore the vasculature that was damaged, and the entire irradiated segment of tissue therefore starves and dies (Kim *et al* 1993).

During the last decade, x-ray microbeam technology, which has been established as a unique tumour therapy concept in medicine, entered the stage of animal experimentation (Slatkin *et al* 1995b). A high spatial resolution of dose transfer to tissue can be achieved using an intensive synchrotron x-ray source. By collimating the source's aperture with a fine pinhole, the beam is shaped to a width of about 30 μm (Slatkin *et al* 1994).

The first suggested application of microbeam radiation therapy (MRT) was as a bundle of pencil microbeams (Slatkin *et al* 1992). The concept of using a microbeam array for treating tumours was tested at the NSLS (National Synchrotron Light Source), with different beams, introducing one beam shifted in steps of hundreds of micrometres. This method led to a new kind of MRT, 'unidirectional MRT' (UMRT) as illustrated in figure 1. Using this method on rats bearing tumours, UMRT was shown to preferentially damage the tumour whilst sparing the normal tissues.

The important UMRT parameters are the dimensions of the array, and the within-array spacing, which together determine the dose level at the edges of the beams. Several UMRT experiments have been made with rodents carrying 9L gliosarcoma (9LGS) tumours, either intracranially (Laissue *et al* 1998) or subcutaneously. Both damaging and sparing effects were recently demonstrated in animals with subcutaneous tumours (Dilmanian *et al* 1999).

In the past, the simulations for the MRT studies implemented a limited configuration of the EGS4 Monte Carlo code that employed prepared code packages, such as INHOM and XYZDOS (Nelson *et al* 1985). Those packages were used as input/output 'black box' code programs for the MRT simulations (Slatkin *et al* 1992, Company and Allen 1998); however, a modification was needed in order to describe the phantom's geometry. A new generation of Monte Carlo simulations was essential to properly simulate the UMRT array of planar beams

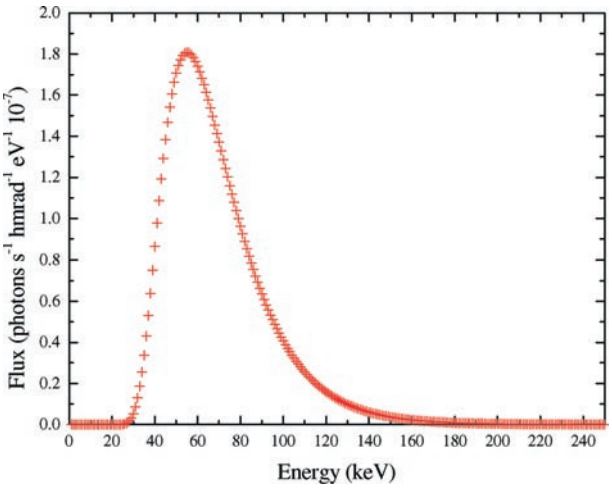

Figure 2. The calculated distribution of the energy output of the NSLS-X17B1 x-ray beam from the SOURCE code (Chapman 1988), using the beam parameters discussed in the text.

and to apply its recent refinements. The simulation aims are to provide a bridge between the current animal studies and human tumour treatments, by exploring the dependence of the dose profile on array beam spacing and the tumour size. An experimental measurement to validate the simulation results can ensure the accuracy of the simulation.

2. Methods

The only previous Monte Carlo study of microbeam therapy was performed with the INHOM code (Slatkin *et al* 1992). A finite cylinder, 16 cm in diameter and 16 cm length, filled with water was used in the first step to compare the previous results of the INHOM code with the new EGS4 user code results. The dose distribution was recorded at 1 μm steps around the x-ray beam by defining a new set of volume-bin cells (voxels). The volume cells (1 μm width) were populated according to coordinates of the deposited energy. Instead of dividing the volume into concentric regions for each of the radii (as defined in the INHOM), we used the bin scoring method to solve the 'crossing border' problem that could be crucial to the electron transport segment (Bielajew and Rogers 1986). However, this method can only be applied inside a homogeneous medium.

2.1. The source

The NSLS X17B1 x-ray beam line was chosen as the UMRT source. The electron-storage-ring current was set for 2.58 GeV at 300 mA. The x-ray beam produced at X17 included the effect of the wiggler magnetic field. The beam was taken as parallel, with approximately 90% linear polarization (Einfeld and Stuck 1980). It was filtered with a copper foil (0.25 mm) and a silicon filter (3.7 mm thickness).

The initial x-ray flux was calculated as an energy distribution function by the synchrotron source calculation code (Chapman 1988); the UMRT simulations used randomly sampled energy from this distribution to form its source (figure 2).

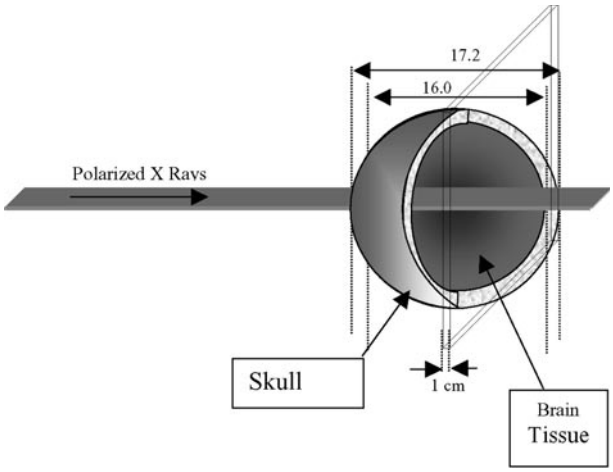

Figure 3. The spherical head phantom, including a skull bone (17.2 cm diameter) and a brain (16 cm diameter). A central section of thickness 1 cm was defined to score absorbed dose profiles.

2.2. Pencil or planar array

The shape of the UMRT experimental source was only tested for a planar-beam grid. Recently, the UMRT approach was expanded, and an advantage was demonstrated in using a rectangular planar-beam grid, which can easily be shaped by a multislit collimator to reduce the loss of the beam's intensity (Slatkin *et al* 1995a). Therefore, a rectangular parallel beam was defined to simulate a planar beam. The dose profile effected by the entire array was specified by the superimposing of the doses, which were calculated separately from a long range of dose profile results. The long-range profile was calculated at 100 μm steps along the whole array field, and the dose was fitted to $1/(1 + bx^c)$ (x is the voxel position along the profile, b and c are parameters, and $c = 1$ was defined for all cases).

2.3. Head phantom

The final UMRT simulation for treating a brain tumour included a head phantom. The head phantom contained two concentric spheres: an inner sphere with a diameter of 16 cm, as the brain tissue region, and an outer sphere, of 17.2 cm radius, to represent the 0.6 mm thick skull region around the brain (figure 3).

This spherical geometry was considered to be a suitable approximated phantom for external x-ray irradiation. For calculating the photon and electron cross sections, the densities of the brain tissue ($\rho = 1.03$ g cm^{-3}) and the skull ($\rho = 1.85$ g cm^{-3}) were taken from ICRP-23 (Snyder *et al* 1975). Table 1 shows the elements included in the calculations, but molecules could only contain up to eight different ones because of the limitation of the current prompt-code (modified LSCAT PEGS package for EGS4). Only atoms with the highest molecular amounts were taken into account.

2.4. The LSCAT package

The Low-energy photon SCATtering expansion package (LSCAT) for the EGS4 code was used in the UMRT simulations (Namito *et al* 1995a). The package was developed to encompass the transport of linearly polarized photons in the EGS4 user code (Hanson 1986,

Table 1. The molecular amounts per atom for brain tissue and for the skull of the phantom.

Atom	Brain tissue ($\rho = 1.03$ g cm^{-3}) (molecular amount)	Skull ($\rho = 1.85$ g cm^{-3}) (molecular amount)
H	0.110 667	0.047 234
C	0.125 420	0.144 330
N	0.013 280	0.041 990
O	0.737 723	0.446 096
Na	0.001 840	0
Mg	0.000 150	0.002 200
P	0	0.104 970
S	0	0.003 150
Cl	0.007 670	0
Ca	0.000 460	0.210 030

Namito *et al* 1993). LSCAT redefined the Compton scattering routine by including the polarized photon-bound Compton scattering equation (Namito *et al* 1995). The Doppler broadening effect was taken into account in the LSCAT routines to fully treat incoherent scattering (Namito *et al* 1995b). Another part of LSCAT contained a modified Rayliegh scattering equation to include the linear polarization characterization (Namito *et al* 1995). An expanded version of the PEGS4 prompt code (included in the LSCAT package), was used to prepare the incoherent scattering functions. The functions were essential in computing the total Compton cross sections of a bound electron, and the Compton profile for the EGS4 calculations. The user-code 'examinnd.mor' in the LSCAT package enabled us to review the photon and electron cross sections, in order to examine the scattering function the materials used.

The photon linear-polarization ratio was defined as 90% in the user code, and the polarization vector was set to be parallel to the width of the beam. There are a few limitations in the LSCAT that might affect the results of the UMRT simulation:

(a) Bremsstrahlung photons are assumed to be unpolarized.
(b) Molecular effects are ignored by using the Compton profile for a free atom.
(c) Compounds or mixtures can only contain up to eight different elements.
(d) The direction of the recoil electron is calculated assuming that the electron is free.

The radiation length of the bremsstrahlung photons was predicted to be shorter than the thickness of the dose profile voxels, due to low-energy photons available in the beam. Only the most important materials in the tissue were put into the simulation because of the limitation on the number of compounds in the code (shown in table 1). LSCAT was tested on a cylindrical water phantom to compare the outgoing scattered spectra parallel and perpendicular to the photon polarization vector of the source (figure 4).

2.5. Photoelectron direction distributions

The default photoelectron direction in the EGS4 code was defined as a forward one, following the direction of interacting photons, and is acceptable for source energies above 1 MeV. The UMRT source emits low-energy photons (below 200 keV); therefore, the photoelectron direction has to be distributed. For a low-energy photon source, the direction of the photoelectrons can be calculated by the relativistic Sauter angular distribution (Sauter 1931):

$$\mathrm{d}N(\mathrm{d}\cos\theta) = \frac{\sin^2\theta}{(1-\beta\cos\theta)^4}[1 + k(1-\beta\cos\theta)] \tag{1}$$

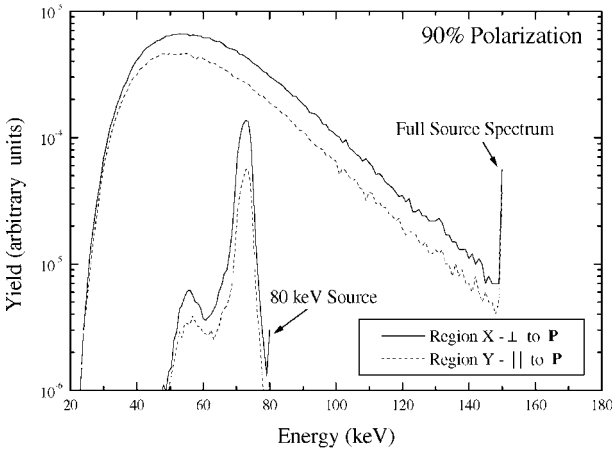

Figure 4. Scattered photon spectra in two different directions, parallel (region Y) and perpendicular (region X) to the photon polarization vector, from a monoenergetic source, and from the full spectrum of the X17B1 source.

where dN is the probability density, θ the electron direction,

$$\beta = \frac{v}{c}$$

$$\gamma = \sqrt{\frac{1}{1-\beta^2}}$$

$$k = \frac{\gamma}{2}(\gamma - 1)(\gamma - 2)$$

v is the electron velocity and c is the speed of light. An approximation for non-relativistic angular distribution ($k \simeq 0$) can be used for very low-energy photoelectrons (below 100 keV). A comparison of the relativistic and non-relativistic equations showed a very small difference in the distribution of photoelectrons at 100 keV (figure 5).

The angular distribution of photoelectron direction was chosen to be used with the extension for the EGS4 code, to include the normalized Sauter distribution (Bielajew and Rogers 1986b).

2.6. The beam's penumbra

The beam's penumbra, a side-effect of the X17B1 beam line, is typically produced in the horizontal direction, and widens the source shape on the surface of the phantom. The planar beam entering the phantom was affected by the penumbra, and yielded S-shaped edges in the dose profile. The S shape was represented by the semiempirical function (Johns and Cunningham 1983)

$$\begin{aligned} f(x) &= 1 - 0.5\exp\left[-\frac{\alpha_1}{p}\left(\frac{w_d}{2} - |x|\right)\right] && \text{for } |x| \leqslant \frac{w_d}{2} \\ &= t + (0.5 - t)\exp\left[-\frac{\alpha_1}{p}\left(|x| - \frac{w_d}{2}\right)\right] && \text{for } |x| > \frac{w_d}{2} \end{aligned} \tag{2}$$

where x is the distance from the centre of the beam (μm) and $w_d = 30$ μm is the beam width at depth d; $p = 3.8$ is the geometric penumbra, which was calculated by multiplying the ratio

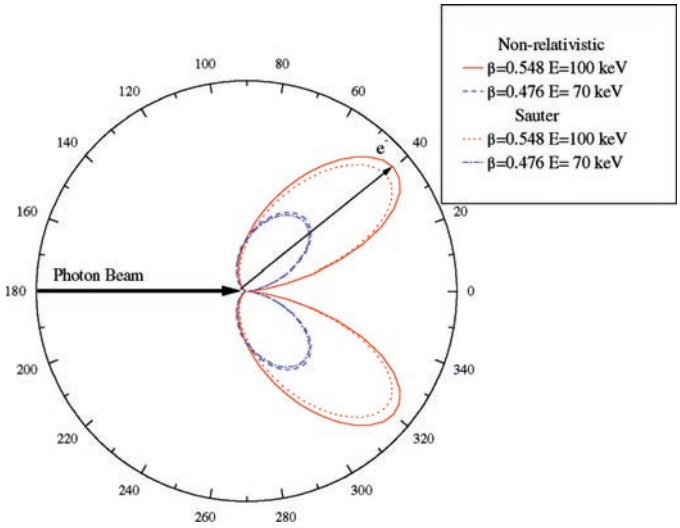

Figure 5. Photoelectron direction resulting from an angular distribution calculation using the Sauter equation, and the non-relativistic equation at 70 keV, and at 100 keV incident photon energies.

of the distance by the width of the source at its origin (0.09 cm). The distances calculated were from the source to the pinhole (28.50 m), and from the pinhole to the phantom surface (12.0 cm). $t = 10^{-4}$ was obtained from experimental measurements of the tail dose level, and $\alpha_1 = 2.5$ from the observed beam edge S shape. The empirical parameters were obtained by MOSFET (metal oxide silicon field effect transistor) microdosimeter measurements in order to attune the results of the EGS4.

2.7. The MOSFET radiation monitor

In recent years, several types of commercial MOSFET radiation monitors have become available for different radiation therapy modalities. The absorbed radiation dose in a MOSFET is proportional to the change in its threshold voltage. A recent innovation in its instrumentation led to the development of an 'edge-on' MOSFET monitor with a micron-thick sensitive silicon oxide volume ($1 \times 200 \times 200$ μm) that measures dose distribution at 1 μm spatial resolution (Rosenfeld *et al* 1996).

The MOSFET chip was mounted inside a gold alloy lid. The lid-side partition of the chip was removed so it was directly exposed to the radiation. The MOSFET detector was encapsulated in a square Lucite case ($16 \times 16 \times 203$ mm), close to the edge of the case (at coordinates 8, 8, 11 mm). The detector materials contained SiO_2, pure silicon and Kovar (a compound of C, Si, Mn, Fe, Co and Ni; $\rho = 8.36$ g cm^{-3}). The 'edge-on' MOSFET detector lay on a moving stage in front of the x-ray, the stage being moved by a stepper motor (Rosenfeld *et al* 1999).

Since the accurate position of the chip on a micron scale was unknown, the first measurements were taken from different locations, finally converging to the centre of the microbeam. The experimental data were collected starting from an arbitrary zero point (± 0.01 μm), and therefore the results were shifted to set them at the same zero point, keeping the original relative distances.

The accessibility to a very high spatial resolution dosimeter, such as MOSFET, provided a convincing confirmation of the findings from the Monte Carlo simulation methods.

3. Results

3.1. Cylindrical water phantom

The first stage phantom was simulated as a cylindrical water volume and was placed in front of a circular pencil beam with a 25 μm diameter, to compare the results of the user code with the INHOM. The second stage of the simulation was carried out under the same conditions, with a rectangular parallel beam of 30 μm $\times$ 3 cm, to compare the effect of the planar beam on the dose profile with that with the pencil beam.

The dose profiles were tallied from a 1 cm thick region in the centre of the phantom. The simulation results introduced a standard deviation of 0.2% at the peak of each profile, while ascending up to 8% at the edge. (Each simulation was preformed with 10^7 histories, and took about 4 h on a Pentium II 200 MHz computer.) Near the inducing cross section, in the range of 25 μm to 75 μm, there was a remarkable difference in the dose height and slope of the two beams, while above 100 μm, the valley did not differ between the planar beam and the pencil beam (figure 6(*a*)). The difference in the lower range, for the current simulation, originated from the specific photoelectron emission and the polarized photon scattering due to the LSCAT transport. In the case of the rectangular beam, a higher dose was realized throughout the entire range. The effect of a high dose in the valley region is an outcome of the beam's rectangular cross-sectional length, which is equivalent to about 1000 adjoining pencil beams.

3.2. Concentric spheres simulating the brain tissue inside a skull

Concentric spheres of brain tissue surrounded by a skull-like symmetrical layer were simulated to create a detailed phantom, appropriate for external dose calculations. The parameters used in the previous section were included in the new geometry and materials definitions. The two kinds of beam shape are shown in figure 6(*b*); a pencil beam with the same radius (12.5 μm), and a rectangular beam (30 μm $\times$ 3 cm) to be used for the dose profiles of the planar array beam.

The effects of phantom geometry and material cannot be seen in the normalized profile shape, but the absolute dose per voxel per incident fluence is 1.4 times lower (the INHOM results showed an absorbed dose per incident fluence of 10^{-17} Gy m^2 at the peak). This finding emphasizes the importance of choosing a more realistic phantom for dose calculations in planning an efficient therapy procedure, especially for brain tumours. The fact that the whole range of the normalized dose profile showed no apparent changes, even after adding a skull to the phantom, led us to conclude that the sharpness of the microbeam was not affected.

3.3. Comparison of peak-to-valley dose ratios

The most significant parameter in the planar array microbeam is the distance between two beams. The design of the beam will have a direct effect on the results of the peak-to-valley dose ratio for a given irradiation area. This ratio is strongly affected by the size of the array, which is set to cover the tumour area and volume. Figure 7 shows a dose profile for two different sizes of array. The peak-to-valley ratio for a 3 $\times$ 3 cm array was about twice that of a 6 $\times$ 6 cm array. However, changing the spacing between beams, in a given array size, can generate a higher peak-to-valley ratio. For example, for a 3 $\times$ 3 cm array, a spacing of 100 μm compared with a spacing of 200 μm increased the peak-to-valley ratio from 5 to 12.5

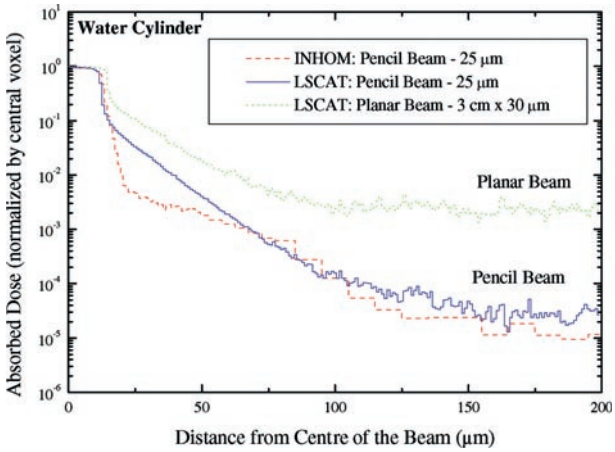

(*a*)

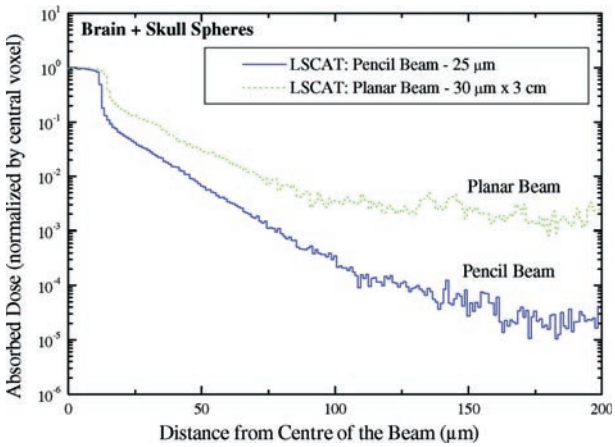

(*b*)

Figure 6. (*a*) EGS4 simulation results for a cylindrical water phantom: INHOM results for a pencil beam at 100 keV compared with the new user code results, using a full-source energy distributed pencil beam. Also shown are the planar beam user code results with a full energy distributed rectangular-beam. (*b*) EGS4 simulation for skull and brain spherical phantom with full-source energy distribution. The results of pencil and planar beam normalized absorbed dose are shown around the induced microbeam region.

times (figure 7(*a*)). The therapy plan for larger tumours may involve a beam array as large as 6×6 cm. The folding ratio for this array will be about 6 with a 200 μm spacing between the centres of the beams. In treating large tumours, the spacing should be increased to fit the tumour size in order to profit from the advantages of the UMRT method.

3.4. MOSFET measurement and simulation

The MOSFET experimental results were factorized to the current readings of the NSLS ring for every data point due to the modest damping of the current during the experiment. The MOSFET readings were determined by the voltage change on the MOSFET, which is proportional to the absorbed dose on the sensitive component. The readings were normalized to a data point in the

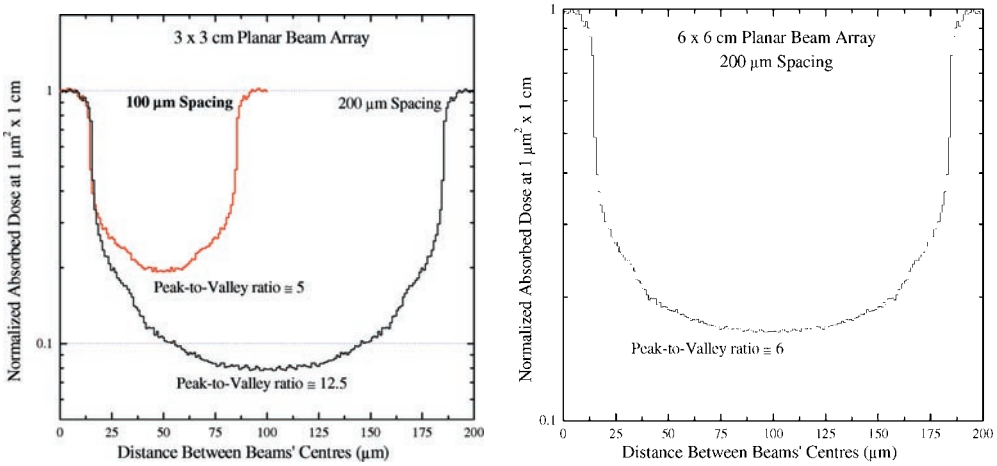

(*a*) (*b*)

Figure 7. (*a*) UMRT peak-to-valley absorbed dose ratios for a small therapy area, 3 × 3 cm, with two different beam spacing of 100 μm, and of 200 μm. The 200 μm spacing array resulted a peak-to-valley ratio of one magnitude. (*b*) UMRT peak-to-valley absorbed-dose ratios for a large therapy area, 6 × 6 cm, showed a half magnitude dose ratio with 200 μm spacing, the minimal recommended spacing for this array size.

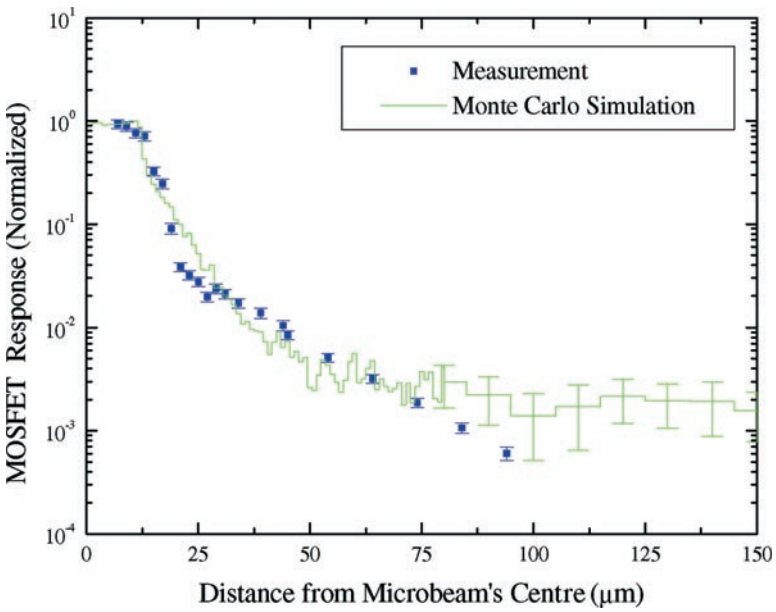

Figure 8. A comparison of the 'edge on' MOSFET experimental results with the EGS4 simulation results along the microbeam profile up to 100 μm. The measured MOSFET response was compared with the simulated absorbed dose, after normalizing the profile results to the maximal dose point.

peak region, and the EGS4 simulation results were normalized using the same profile point. In figure 8, both the normalized experimental results and the normalized simulation results are shown within a range of 90 μm from the centre of the microbeam.

4. Conclusions

The UMRT method was tested with Monte Carlo simulations using a rectangular beam, and was found to be a very promising modality to treat brain tumours due to the high dose slope around the microbeam. The microbeam was produced at the NSLS with a high intensity and photon polarization, suitable for the experimental stage of our work. A simplified x-ray device will be designed as we advance to the clinical stages of the project. To proceed with developing the UMRT method, it is essential to use an alterable user code for the Monte Carlo simulations. The change in the absolute absorbed dose caused by the characteristics of the phantom, led us to conclude that it will be necessary to change its geometry in UMRT simulations for treating different organs.

The peak-to-valley ratio of the absorbed dose was found to be a critical parameter in planning tumour therapy. The ratio was affected by the size of the UMRT array and by the beam spacing. Beam spacing is the parameter used to reduce the dose level between the beams of the array. In treating large tumours, the spacing should be increased to fit the size of the tumour to fully utilize use the advantages of the UMRT biological method.

The experimental results showed that the MOSFET was a useful x-ray microdosimetery device for microbeam therapy, with a rapid response and a linear output-to-dose calibration. Comparing the MOSFET measurements with the EGS4 simulations (including the LSCAT), showed, for the first time, an acceptable agreement at a micrometric scale. The MOSFET experiment provided consistent results between EGS4 simulations and measurement with a benchmarked dosimeter (Rosenfeld *et al* 1996), providing an indication that the simulation will be appropriate to patient dosimetry. Advanced MOSFET experiments will help us elucidate the depth dependence of the shape and magnitude of the dose profile in tissue-like phantoms.

Acknowledgments

This research was partly supported by the US Department of Energy, and also by the Children's Brain Tumor Foundation. We thank Avril Woodhead for her comments on this manuscript.

References

Bielajew A F and Rogers D W O 1986a PRESTA: the parameter reduced electron-step transport algorithm for electron Monte Carlo transport *National Research Council Report* PIRS-042 (Ottawa: NRCC)

——1986b Photoelectron angular distribution in the EGS4 code system *NRCC Internal Report* PIRS-0058

Chapman L D *et al* 1988 The SOURCE code for synchrotron x-ray source calculations *Nucl. Instrum. Methods Phys. Res.* A **266** 191–4

Company F Z and Allen B J 1998 Calculation of microplanar beam dose profile in a tissue/lung/tissue phantom *Phys. Med. Biol.* **43** 2491–501

Dilmanian F A *et al* 1999 Spatially fractionated, unidirectional microbeam radiation therapy of rat brain gliosarcomas *4th Ann. Meeting of the Society for Neuro-Oncology* (*Neuro-Oncology* **1** 307)

Einfeld D and Stuck D 1980 Synchrotron radiation as an absolute standard source *Nucl. Instrum. Methods Phys. Res.* **172** 101–6

Hanson A L 1986 The calculation of scattering cross sections for polarized x-rays *Nucl. Instrum. Methods Phys. Res.* A **243** 583–98

Johns H E and Cunningham J R 1983 *The Physics of Radiology* 4th edn (Springfield, IL: Thomas)

Kim K J, Winer B, Li J, Armannini M, Gillett N, Phillips H S and Ferrara N 1993 Inhibition of vascular endothelial growth factor-induced angiogenesis suppresses tumor growth *in vivo Nature* **362** 841–4

Laissue J A *et al* 1998 Neuropathology of ablation of rat gliosarcomas and contiguous brain tissues using a microplanar beam of synchrotron-wiggler-generated x rays *Int. J. Cancer* **78** 654–60

Namito Y, Ban S and Hirayama H 1993 Implementation of linearly-polarized photon scattering into the EGS4 code *Nucl. Instrum. Methods Phys. Res.* A **332** 277–83

Namito Y, Ban S and Hirayama H 1995a Compton scattering of 20- to 40-keV photons *Phys. Rev.* A **51** 3036–43
——1995b LSCAT: low-energy photon-scattering expansion for the EGS4 code *KEK National Laboratory for High Energy Physics Internal Report* 95-10
Nelson W R, Hirayama H and Rogers D W O 1985 The EGS4 code system *SLAC Report* 265
Rosenfeld A *et al* 1996 MOSFET simultaneous micro-macro dosimetry *IEEE Trans. Nucl. Sci.* **43** 2693–700
Rosenfeld A, Kaplan G, Kron I, Allen B, Dilmanian A, Orion I, Ren B and Lerch M 1999 MOSFET dosimetry of an x-ray microbeam *IEEE Trans. Nucl. Sci.* **46** 1774–80
Sauter F 1931 Uber den atomaren Photoeffekt in der K-Schale nech der relativistischen Wellenmechanik Diracs *Ann. Phys.* **11** 454–88
Slatkin D N *et al* 1995a Design of a multislit, variable width collimator for microplanar beam radiotherapy *Rev. Sci. Instrum.* **66** 1459–60
Slatkin D N, Dilmanian F A and Spanne P 1994 Method for microbeam radiation therapy *US Patent* 5,339,347
Slatkin D N, Spanne P, Dilmanian F A, Gebbers J-O and Laissue J A 1995b Subacute neuropathological effects of microplanar beams of x-rays from a synchrotron wiggler *Proc. Natl Acad. Sci., USA* **92** 8783–7
Slatkin D N, Spanne P, Dilmanian F A and Sandborg M 1992 Microbeam radiation therapy *Med. Phys.* **19** 1395–400
Snyder W S, Cook M J, Nasset E S, Karhausen L R, Howells G P and Tipton I H 1975 Report of the Task Group on Reference Man *International Commission on Radiological Protection Publication* 23 (Oxford: Pergamon)